Shape anisotropy induced field-free switching and enhancement of dampinglike field in Pt/Co/PtMn heterostructures with a wedged ultrathin antiferromagnetic PtMn layer

Birui Wu [1,2,*] Menghao Jin,[1,*] Ziji Shao,[1] Haodong Fan,[1] Jiahong Wen,[1] Hai Li,[1] Changqiu Yu,[1,†] Bo Liu,[3,‡] and Tiejun Zhou [1,2,§]

[1]*School of Electronics and Information Engineering, Hangzhou Dianzi University, Hangzhou, Zhejiang 310018, China*
[2]*College of Information and Mechanical Electrical Engineering, Ningde Normal University, Ningde 352100, China*
[3]*Key Laboratory of Spintronics Materials, Devices and Systems of Zhejiang Province, Zhejiang 311305, China*

(Received 24 March 2023; revised 24 June 2023; accepted 28 July 2023; published 11 August 2023)

Current-induced spin-orbit torque (SOT) switching of perpendicular magnetization requires an additional symmetry breaking, calling for modifications of the conventional SOT devices. Here, we have systematically investigated current-induced magnetization switching and dampinglike field in Pt/Co/PtMn trilayer films with a wedged ultrathin antiferromagnetic (AFM) PtMn layer. The symmetry is broken by the effective shape anisotropy in the wedged ultrathin AFM PtMn layer, resulting in the observed field-free SOT switching. Quantitative characterization manifests that the dampinglike (DL) field is boosted up to 30% through wedging the AFM PtMn layer. Additional experiments with *in situ* magnetic field and micromagnetic simulations indicate the canting of spins caused by the wedge shape accounts for the observed field-free switching and enhancement of SOT efficiency. Our findings provide an easier approach to field-free switching and H_{DL} enhancing for magnetic memory devices with high density and low power consumption.

DOI: 10.1103/PhysRevB.108.054417

I. INTRODUCTION

Spin-orbit torque has great potential to enable ultrafast operating speed and ultralow-power magnetic memories and logic devices for many key electronics applications [1–5]. The charge current passing through the HM (heavy metal) [6–12] generates a nonequilibrium spin density at the HM/FM (ferromagnet) interface via the spin Hall effect (SHE), that produces torques (the dampinglike (DL) torque $\tau_{DL} \sim m \times (\sigma \times m)$ and the fieldlike torque $\tau_{FL} \sim (\sigma \times m)$ acting on the adjacent FM layer [13]. However, in such material systems with perpendicular anisotropy, an in-plane external magnetic field is typically required to assist spin-orbit torque-driven switching, which is an obstacle for practical applications [14]. Field-free magnetization switching is critical towards integrated spin-orbit torque (SOT)-driven magnetic random-access memory with perpendicular magnetic anisotropy [15]. In addition, the switching current in SOT devices needs to be continuously reduced for lower power consumption.

The symmetry breaking is crucial to realize the deterministic field-free SOT switching, such as by effective in-plane exchange bias [6,13,16,17], tilted anisotropy [18], stacks with interlayer exchange coupling [19–22], chiral symmetry breaking [23], and lateral wedged structure. A tilt in the anisotropy axis could be realized using the sputtering process by wedge-shaped oxide layer [24–26], ferromagnet layer [14,27,28], Mo layer [29], dusting layer [30], light-metal layer [31], and heavy-metal layer [32,33].

Previous studies have shown the presence of missing coordination and uncompensated magnetization in antiferromagnets with size down to a few nanometers [34–38]. Such missing coordination and uncompensated magnetization, coupled with geometric asymmetry (such as wedged ultrathin film), might generate an effective shape anisotropy that magnetically breaks the symmetry, leading to field-free switching of perpendicular magnetization and the modification of SOT efficiency. Here, we studied the current-induced magnetization switching and dampinglike SOT field in perpendicularly magnetized Pt/Co/PtMn trilayer films with wedged ultrathin AFM PtMn layer. The wedged PtMn layer was deposited at an oblique angle by stopping the substrate rotation. A deterministic field-free SOT switching was observed due to the effective shape anisotropy resulting from the combined effect of the missing coordination, uncompensated magnetization, and the wedged shape. We further found that the dampinglike effective fields (H_{DL}) could be increased by an amount of up to 30% with the wedged PtMn. The tilted spin texture at the Co/PtMn interface caused by wedged PtMn may play a role in the field-free switching and enhancement of SOT efficiency. Our results may advance SOT-based spintronic devices towards high-density and low-power memory and logic applications.

II. SAMPLE PREPARATION

The samples were deposited on thermally oxidized Si/SiO_2 substrates by magnetron sputtering using an AJA International physical vapor deposition system at room temperature under a base pressure of better than 4×10^{-8} mTorr.

*These authors contributed equally to this work.
†cqyu@hdu.edu.cn
‡liubo@spinlab.cn
§tjzhou@hdu.edu.cn

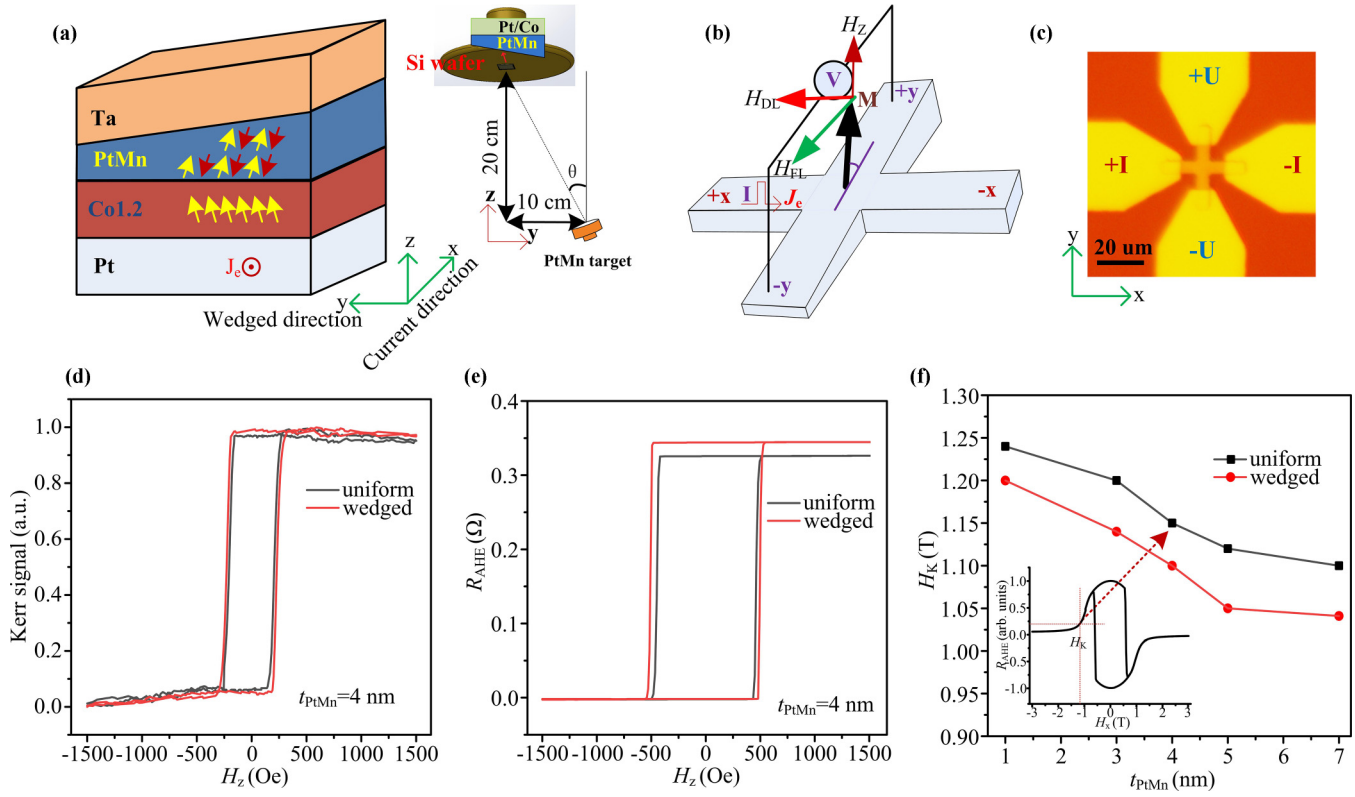

FIG. 1. (a) Illustration of lateral symmetry breaking by wedged PtMn layer. (b) Schematic of Hall bar and measurement configuration. I and V stand for pulse current and Hall voltage parameters, respectively. H_{DL}, H_{FL}, and H_Z are dampinglike, fieldlike, and effective out-of-plane magnetic fields, respectively. M is unit vector of magnetization. (c) Optical micrograph of fabricated 5-μm × 5-μm Hall bar device. (d) Normalized out-of-plane field (H_Z)-dependent Kerr signals (a.u.) of sample for uniform (black line) and wedged PtMn (red line) (indicated by uniform/wedged in all figures). (e) Hall resistance R_{AHE} as function of out-of-plane field H_Z for uniform (black line) and wedged PtMn (red line) Hall bar samples. (f) Perpendicular anisotropy field H_k as function of PtMn thickness for uniform (black line) and wedged PtMn (red line) ($t_{PtMn} = 1 \sim 7$ nm) samples. Inset shows measurement carried out to extract H_k from plot of anomalous Hall resistance (R_{AHE}) as function of external in-plane magnetic field H_x for 4-nm wedged PtMn layers.

The film's layer stack was Ta(1)/Pt(5)/Co(1.2)/PtMn(t)/Ta(2) (thickness in nanometers) from the substrate side, and the thickness of PtMn, t_{PtMn}, varied from 1 to 7 nm. To study the influence of the wedged PtMn on the spin-orbit torque, the PtMn layer was deposited at an oblique angle without rotating the substrates, yielding a continuous gradient of thickness along the length of the sample [inset in Fig. 1(a)]. For the PtMn layer with uniform thickness, the substrates were rotated during the deposition.

A schematic illustration of sample structure is shown in Fig. 1(a). A canted spin texture [Fig. 1(a)] was proposed for the wedged ultrathin AFM PtMn layer due to a combined effect of the missing coordination, the noncompensated spins, and the wedged shape. Generally, as an AFM's dimension scales down to a few nanometers, the missing coordination and the noncompensated spins come in to play, due to size effect [36,38], through the modification of exchange interactions for the surface spins, leading to spin canting (noncollinear spins) at the surface/interface. A wedged shape breaks the lateral symmetry and ensures that the net effect does not cancel out and therefore results in an ordered spin canting at the surface/interface. The surface spin canting may propagate throughout the nanometer AFM film via exchange coupling as proposed in Fig. 1(a) and will be verified by micromagnetic simulations [Figs. 6(a) and 6(b)]. In effect, the coupled effects from the missing coordination, noncompensated spins, and wedged shape can be equivalent to an asymmetric shape anisotropy due to demagnetizing effect [34–39], which tilts the moments in the AFM layer. Such AFM spin canting causes a slight spin tilting of the Co layer through interlayer exchange coupling.

Figure 1(b) presents the schematic of the Hall bar and the measurement configuration. The arrows depict the case where mirror symmetry is broken only about the y-z plane. In this case, the symmetry breaking results in current-induced SOTs, which, to quadratic order in m, consist of the dampinglike torque $\tau_{DL} \sim m \times (\sigma \times m)$ and fieldlike (FL) torque $\tau_{FL} \sim (\sigma \times m)$ [24].

We patterned the films into 5-μm × 5-μm Hall bar structures by using photolithography and Ar ion milling. Electrode pads with Ti (10 nm)/Au (50 nm) were fabricated for electrical measurements, as shown in Fig. 1(c).

III. RESULTS AND DISCUSSION

A. Magnetic characterization

Figure 1(d) shows a representative out-of-plane hysteresis loop obtained by the magneto-optical Kerr effect (MOKE) for

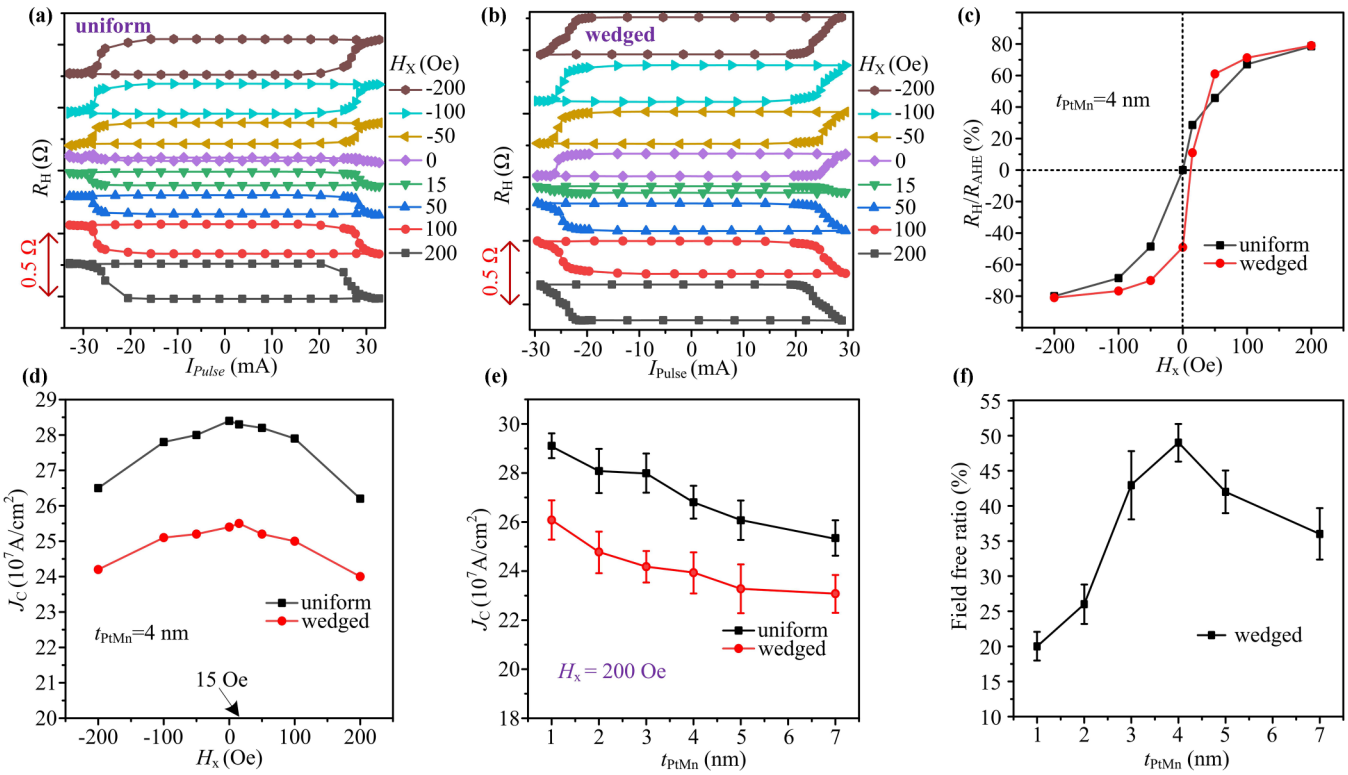

FIG. 2. Current-induced magnetization switching for devices with 4-nm uniform (a) or wedged (b) PtMn layer measured under varied auxiliary field H_x from −200 to +200 Oe; $\Delta R_H/R_{\rm AHE}$ (c) and critical switching current density J_c (d) as function of auxiliary field for devices with 4-nm wedged or uniform PtMn layers; (e) Critical switching-current density J_c for wedged or uniform PtMn layers as function of PtMn thickness under auxiliary field $H_x = 200$ Oe; (f) field-free switching ratio ($\Delta R_H/R_{\rm AHE}$) as function of wedged PtMn thickness. Error bars in (e) and (f) correspond to standard deviation of average value.

the trilayer samples [Ta(1)/Pt(5)/Co(1.2)/PtMn(4)/Ta(2)] with uniform/wedged deposited PtMn layers, from which film's perpendicular magnetic anisotropy (PMA) is verified.

Figure 1(e) shows the typical anomalous Hall resistance, $R_{\rm AHE}$, as a function of out-of-plane field H_Z for devices with uniform/wedged PtMn. Similar to the MOKE results, the $R_{\rm AHE}-H$ loops showed clear PMA for both devices, while the wedged PtMn trilayer slightly changed the coercivity and $R_{\rm AHE}$ (red line versus black line). A comparison of Figs. 1(d) and 1(e) reveals a significant increase in coercivity after the sheet films were patterned into micrometer-sized Hall devices. The patterning process introduced various types of defects such as damaged magnetics and physical roughness at the edges. These defects serve as pinning centers during the magnetization reversal process, resulting in a higher coercivity, as evidenced after considering the current-shunting effect by our observations.

To extract the effective perpendicular magnetic anisotropy field (H_k), we measured the Hall resistance, R_H, as a function of an in-plane magnetic field applied along the x axis. Generally, as the applied in-plane field, H_x, is larger than the anisotropy field H_k, the magnetization will lie in the plane along the x axis, resulting in a nearly zero Hall resistance. The H_k can be estimated as the point where the normalized in-plane component of the magnetization, $m_x = \sqrt{1-m_z^2}$, reaches 0.98 [25,30], as illustrated as an inset in Fig. 1(f). Figure 1(f) shows how the H_k changes with PtMn thickness for the uniform (red circles) and wedged (black squares) samples. It was found that the H_k decreased with the PtMn thickness, while the wedged PtMn layer further reduced the H_k at a percentage of about 5 to 10%.

B. Spin-orbit torque switching

The anomalous Hall resistance (R_H) was used to determine the spin-orbit torque switching of magnetization between up and down states. A dc pulse current, I, along the x direction with a pulse width of 30 μs was applied to drive the magnetization switching. The current pulse was swept from negative to positive and back to negative. After each current pulse (5 s), the transverse voltage R_H was measured by sending a small read current (10 μA) to the current channel of the Hall bar.

The switching loops under different in-plane auxiliary H_x along the charge-current direction for the two PMA heterostructure devices with 4-nm uniform or wedged PtMn are shown in Figs. 2(a) and 2(b), respectively. For devices with wedged PtMn layer, the dc pulse current, I, was applied under different auxiliary fields, where a field-free switching loop is clearly observed. In contrast, the magnetization of the FM (Co layer) with uniform PtMn layer could not be switched without an external field, regardless of the direction of pulse current. If the magnetization of Co was tilted away from the z axis, the symmetry between up and down magnetization states was effectively broken, and field-free SOT switching could be realized by the conventional dampinglike SOT

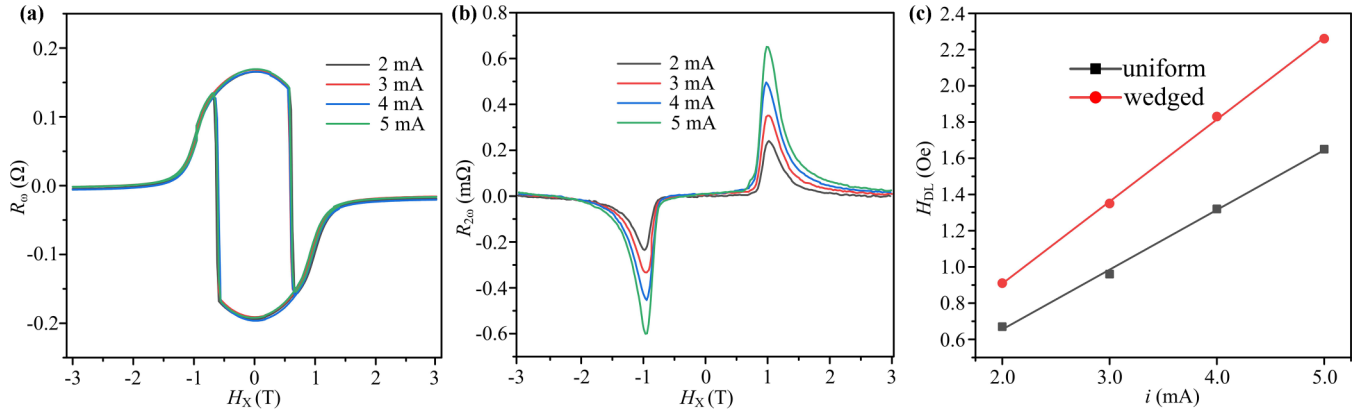

FIG. 3. Estimation of SOT effective field using harmonic Hall signals for Hall bar device with $t_{PtMn} = 4$ nm. (a) First- and (b) second-harmonic Hall signal as function of longitudinal magnetic field H_x for different ac. (c) Linear fitting of dampinglike effective field H_{DL} vs applied ac current for uniform PtMn layer (black squares) and wedged PtMn layer (red circles).

scenario due to the in-plane component of magnetization [40]. For the devices with wedged PtMn, as shown in Fig. 1(a) and previously discussed, an equivalent shape anisotropy tilted the spins of both the PtMn and Co layers away from the z direction, which combined with spin Hall effect from the bottom Pt layer, leading to the observed field-free SOT switching [Fig. 2(b)].

Figure 2(c) shows the switching ratio ($\Delta R_H/R_{AHE}$) as a function of auxiliary field H_x for the devices with 4-nm wedged (red circles) or uniform (black squares) PtMn layers. The positive and negative values of ΔR_H correspond to different switching polarities. It is seen that the switching ratio of the device showed an obvious shift for samples with wedged PtMn layer, which corresponded to an in-plane effective field of 15 Oe along the J_c direction.

For the two devices with 4-nm wedged (red circles) or uniform (black squares) PtMn layers, the critical switching current densities J_c, defined as the current density at which 50% switching happens under different auxiliary fields, are summarized in Fig. 2(d). For both devices, J_c decreased with increasing auxiliary field, which is a typical characteristic of SOT-induced magnetization switching [41]. The critical switching current of the wedged PtMn layer was reduced by an amount of about 12% compared to the uniform PtMn layer. Figure 2(e) shows how the switching current density, J_c, measured under an auxiliary field of 200 Oe, changed with PtMn thickness for devices with wedged (red circles) or uniform (black squares) PtMn layers. The J_c decreased with the increasing PtMn thickness regardless of wedged or uniform PtMn layers, being a similar trend as that observed for H_k as a function of PtMn thickness [Fig. 1(f)]. In addition, the devices with the wedged PtMn layers had lower J_c and the reduction reached about $12 \pm 3\%$.

Figure 2(g) shows the field-free switching ratio, $\Delta R_H/\Delta R_{AHE}$, as a function of wedged PtMn thickness. The $\Delta R_H/\Delta R_{AHE}$ increased with the wedged PtMn thickness, and peaked at 4-nm PtMn with a value of about 49%. Further increasing wedged PtMn thickness resulted in a decrease of field-free switching ratio. However, no field-free switching was observed for all the devices with uniform PtMn layers. On the other hand, applying an *in situ* field would induce spin tilting in samples with uniform PtMn layer as previously reported [42], where a field-free switching and a similar trend of $\Delta R_H/\Delta R_{AHE}$ and J_c vs PtMn thickness are observed.

C. Quantitative evaluation of the SOT effective field

We quantified the SOT effective field of the Pt/Co/PtMn heterostructure devices via harmonic Hall voltage measurements. An external field, $H = 3$ T, was applied in the x-z plane at a polar angle of $\theta_H = 87^\circ$, and an ac, $i = I_0 \sin(\omega t)$, was applied along the x direction, which generated an alternating SOT to oscillate the magnetic moment around H_x. The current flowing parallel to the interface plane with structural inversion asymmetry induced two spin torques: the fieldlike field (H_{FL}) and dampinglike field (H_{DL}). Then, the in-plane field dependence of second-harmonic signal [17,43,44] $R_{xy}^{2\omega}$ at large field was obtained as

$$R_{xy}^{2\omega} = \frac{R_{AHE}}{2}\frac{H_{DL}}{H_x - H_k} + \frac{R_{PHE}}{2}\frac{H_{FL}}{H_x} + R_{SSE+ANE}.$$

The parameter $R_{PHE}(\sim 0.02\,\Omega) \ll R_{AHE}(\sim 0.32\,\Omega)$, where R_{AHE} and R_{PHE} are the anomalous Hall signal and planar Hall signal, respectively. We therefore neglect the second term in the equation. $R_{ANE+SSE}$ is the thermal contribution from anomalous Nernst (ANE) and spin Seebeck effects (SSE). The $R_{2\omega}$ as a function of $\frac{1}{2}\frac{R_{AHE}}{H_x - H_k}$ is plotted in Fig. S1 in Supplemental Material [45]. The fitting process was performed within the high-field range of $H_k \leqslant H_x \leqslant 3$ T to ensure the determination of a reliable effective field. The fitting parameter $R_{ANE+SSE}$ was around 0.023 mΩ, indicating a very small and negligible contribution from ANE, compared to the AHE contribution, which is a few orders larger.

Figures 3(a) and 3(b) show the typical field dependence of the first- and second-harmonic Hall signals for films having wedged PtMn layers at $t_{PtMn} = 4$ nm, measured under different ac current (2, 3, 4, and 5 mA), respectively. Based on the harmonic Hall voltage measurements, the current-induced dampinglike field, H_{DL}, can be calculated. Figure 3(c)

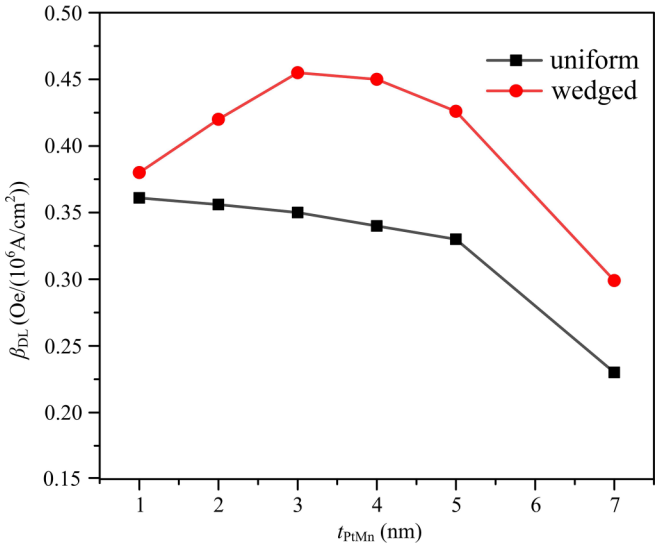

FIG. 4. Dampinglike effective field per current density β_{DL} as function of PtMn thickness for uniform (black squares) and wedged PtMn layer (red circles).

shows such obtained effective field H_{DL} as a function of applied ac for films having wedged and unform PtMn layers at $t_{PtMn} = 4$ nm. Based on Fig. 3(c), the SOT effective field per current density, $\beta_{DL} = H_{DL}/J$, could be determined.

Figure 4 illustrates how the β_{DL} changes with PtMn thickness for devices with uniform (black solid squares) and wedged (red solid circles) PtMn layers without considering the current-shunting effect. For devices with wedged PtMn, β_{DL} increased with PtMn thickness first, peaked at PtMn = 3 nm, and then decreased with PtMn thickness. When the thickness of the PtMn layer was thick enough, the efficiency β_{DL} could be reduced by the current divider in the trilayer system. For devices with unform PtMn, β_{DL} kept decreasing as PtMn thickness increased. Most interesting, β_{DL} was much enhanced with wedged PtMn layer and the enhancement could be up to 31% at PtMn = 3 nm. After considering the current-shunting effect, as shown in Fig. S2 of Supplemental Material [45], the β_{DL} was slightly reduced and the general trend of β_{DL} vs PtMn thickness was moderately modified, while the enhancement of β_{DL} through wedging the PtMn layer was the same as that without considering the current-shunting effect. The wedge-induced β_{DL} enhancement was similar to what was previously reported, where a β_{DL} boosting was observed for devices with a uniform PtMn layer through the application of an *in situ* field [42]. Such β_{DL} boosting may be related to the spin canting of AFM PtMn layer that forms a noncollinear spin texture at the Co/PtMn interface [Fig. 1(a)]. As reported previously, such noncollinear spin texture may enhance the spin reflection at the interface, while the reflected spins would act back on the local spins, leading to a higher effective field as observed.

D. The effects of *in situ* magnetic-field directions on the SOT efficiency in wedged PtMn devices

In order to confirm the above hypothesis, the SOT efficiency should be measured with different spin-tilting angles

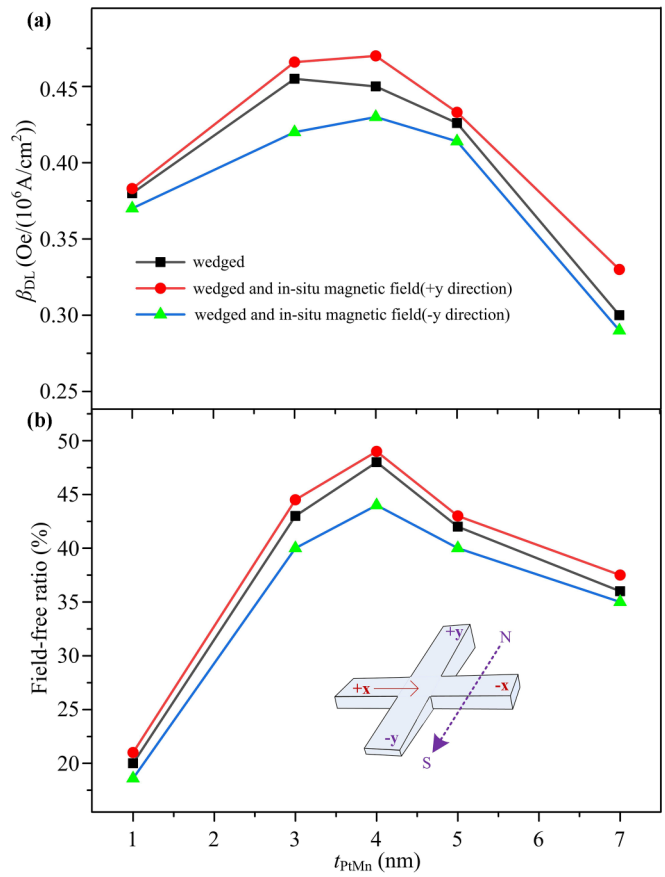

FIG. 5. (a) Dampinglike effective field per current density, β_{DL}, and (b) field-free switching ratio as function of wedged PtMn thickness for devices prepared with presence of *in situ* field along $+y$ (red circles) and $-y$ directions (green triangles) and devices prepared without *in situ* field (black squares). Inset shows direction of *in situ* magnetic field.

in the wedged PtMn layer, which can be tuned through the application of an *in situ* magnetic field along $+y$ and $-y$ directions during film deposition process, respectively. We therefore conducted further experiments using devices with wedged PtMn layer prepared in the presence of an *in situ* magnetic field along the $+y$ direction (red round) and $-y$ direction (green triangle), respectively, during sputtering. The sample depositions followed what was reported in Ref. [42]. The $\pm y$ direction *in situ* field slightly changed the spin directions of the PtMn layer, leading to the change of the magnetization (spin-) tilting angle.

As shown in Fig. 5(a), for all the studied thicknesses of wedged PtMn, β_{DL} was enhanced for devices prepared with the presence of $+y$ direction *in situ* field, while it was reduced for devices prepared with $-y$ direction *in situ* field, compared with devices prepared without the *in situ* field. The $\pm y$ direction *in situ* fields increased or decreased the spin canting angle of the wedged PtMn layer that enlarged or reduced the relative angle between the spins of Co and PtMn layers, leading to the enhancement or reduction of the β_{DL}. In other word, the β_{DL} became higher with increasing absolute value of the tilting angle in PtMn layer. Meanwhile, the field-free switching ratio had a similar trend, as shown in Fig. 5(b).

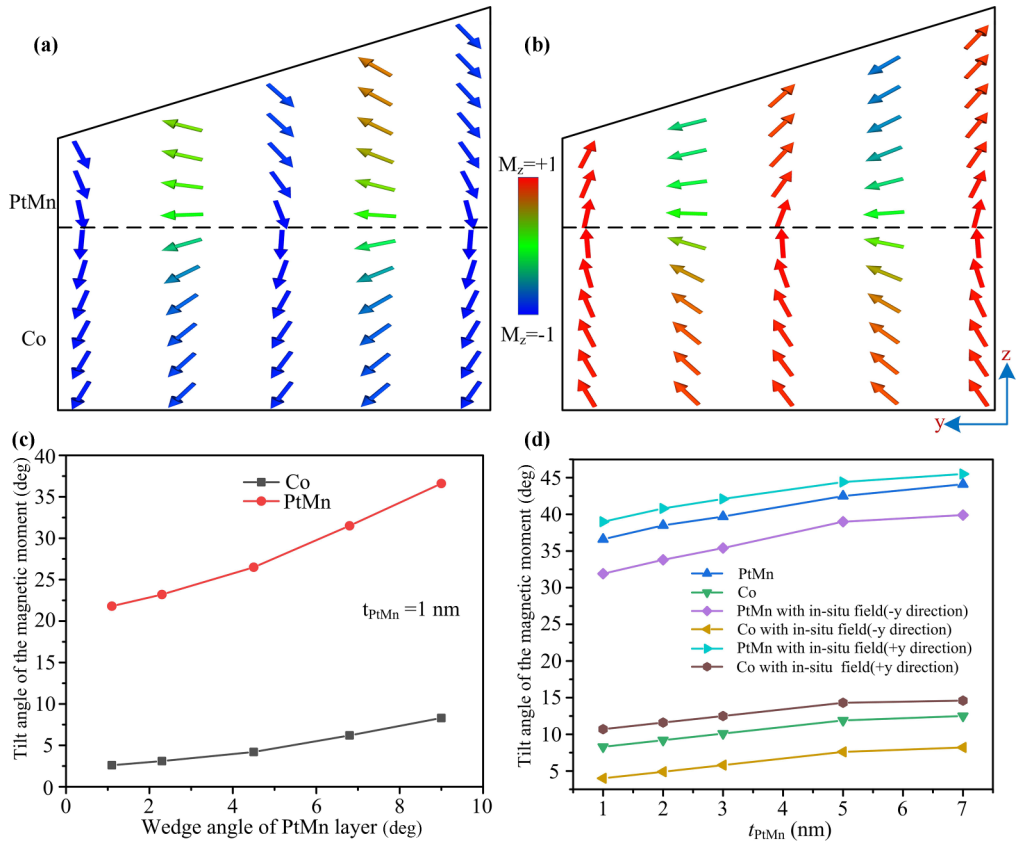

FIG. 6. (a) Cross-sectional snapshot of up state in equilibrium for $t_{PtMn} = 1$ nm without *in situ* magnetic field. (b) Down state in equilibrium. Moment is represented by arrow. Color of arrow reflects value of M_z. (c) Magnetic moment inclination angles of Co and PtMn under different PtMn wedge angles. (d) Tilt angles of PtMn and Co layers vs the PtMn thickness after relaxation for films prepared with/without *in situ* magnetic field. Positive angle is toward $+x$ direction.

E. Micromagnetic simulation

The micromagnetic simulations were further performed to understand the underlying mechanism of the field-free magnetization switching and the enhancement of SOT efficiency by the wedged PtMn layer. The Landau-Lifshitz-Gilbert equation was carried out with a cell size of $1 \times 1 \times 0.2\,\text{nm}^3$ in $5 \times 5\text{-nm}^2$ rectangle sample area. The height of Co layer was fixed at 1.2 nm, the same as the experimental value. The average heights of the wedged PtMn layer varied from 1 to 7 nm, corresponding to different thickness samples.

According to the illustration shown in the inset of Fig. 1(a), the tilt angle for oblique sputtering of devices was small. Therefore, the wedge angle of the PtMn layer was so small that it was difficult to perform simulations. In order to qualitatively analyze the influence of the wedged PtMn layer, the angle of the wedged PtMn layer was set from about 1° to 9°. The fcc (111) texture of PtMn layer was confirmed by x-ray-diffraction (XRD) measurement (see Fig. S3(a) in Supplemental Material [45]). The sketch structure of the PtMn(111)/Co film with close-packed structure is shown in Fig. S3(b). As the *C*-type antiferromagnetism, the intraplane coupling of PtMn layer is antiferromagnetic, while its interplane coupling is ferromagnetic. The antiferromagnetic layer is regarded as two ferromagnetic sublattices where the magnetization of one sublattice is antiferromagnetically coupled to another sublattice, and the dynamics are solved separately for each cell [50–53].

The saturation magnetization of Co was fixed at 9×10^5 A/m (experimental value), while its H_k varied according to the data presented in Fig. 1(f). The anisotropy constant for PtMn was $8 \times 10^5\,\text{J/m}^3$. If the *in situ* field was zero, the direction of anisotropy for uniform PtMn was along the z axis. Otherwise, the direction depended on the ratio of applied *in situ* in-plane field over the H_k of Co/Pt. The interlayer exchange coupling was assumed to be 0.8×10^{-11} J/m, which was smaller than both 1.3×10^{-11} J/m of Co and -1.0×10^{-11} J/m of PtMn [42,54,55]. The Gilbert damping constant was 0.1 and spin Hall angle was 0.11 for the whole magnetic system [56].

Figures 6(a) and 6(b) depict the cross-sectional snapshots of the up and down states in the equilibrium for $t_{PtMn} = 1$ nm without the *in situ* magnetic field, respectively. The arrow represents the magnetic moment. The color of the arrow reflects the value of M_z. It was seen that the spins of AFM PtMn layers were tilted away from the film normal caused by the wedged PtMn, which verifies that proposed in Fig. 1(a) in a more detailed way. The spins of Co layer were canted as well due to the exchange coupling with the PtMn layer. The magnetic moment tilt angles of the ferromagnetic layer Co and the antiferromagnetic layer PtMn versus the wedge angle

of PtMn layer are shown in Fig. 6(c). The wedge angles of PtMn layer with $t_{PtMn} = 1$ nm varied from about 1° to 9°. It indicates that the magnetic moment tilt angles of the two layers both increased with the increasing wedge angle of PtMn layer. The tilt angle of PtMn layer was much larger than that of Co layer.

As a typical representative, Fig. S4 shows the simulated current-induced magnetization switching for $t_{PtMn} = 1$ nm (see Fig. S4 in Supplemental Material [45]). Without any auxiliary field, the normalized moments can be flipped up and down by positive and negative pulse currents, respectively. The results are similar for different thicknesses of PtMn. In Fig. 6(d), the absolute tilted angles for both Co and PtMn layers after relaxation are plotted versus the thickness of PtMn layer prepared with/without the *in situ* magnetic field of $\pm y$ directions. The tilted angles of Co and PtMn were calculated by averaging the directions of moments in the corresponding layers. The absolute values of tilting angles for Co and PtMn layers both increased with the increasing thickness of PtMn. The angles for Co layers were much smaller than those for PtMn layers. The angles for both layers almost reached saturation as the thickness of PtMn $\geqslant 5$ nm. The *in situ* magnetic fields of positive and negative y directions could increase and decrease the tilting angles by changing the direction of anisotropy in the PtMn layer, respectively. Those simulation results agree with the experimental observation shown in Figs. 5(a) and 5(b).

As shown in Fig. 6(c), the tilt angles of PtMn and Co layers continued to decrease but in a much slower way as the wedge angle was smaller than 2°, showing a saturation behavior. Physically, the tilt angles of PtMn and Co layers were mainly determined by system's total energy that mainly included the anisotropy energy, the exchange energy, and the effective demagnetization energy due to coupled effect of missing coordination, noncompensated spins, and the wedged shape. Therefore, additional simulations of the anisotropy energy, the exchange energy, and the effective demagnetization energy as a function of wedge angles were carried out to understand the underlying physics. The calculated anisotropy energy and the effective demagnetization energy are shown in Fig. S5 of Supplemental Material [45], while the calculated change of exchange energy was about two orders lower than the other two energy terms, showing a negligible effect of wedging on exchange energy. It is seen that the two energy terms exhibited a similar trend as the tilt angles of PtMn and Co layers did as the wedge angle varied. Especially as wedge angle $<2°$, a saturation of the anisotropy and effective demagnetization energy was seen. Such saturation behavior indicated that the system's energy changed little as the wedge angle was continuously reduced to smaller than 2°. The tilt angle of both PtMn and Co layers therefore showed a similar saturation behavior as shown in Fig. 6(c). On the other hand, the simulation showed that as long as there was a slight wedge angle in the sample the symmetry would be broken, and field-free switching of perpendicular magnetization would happen. Therefore, an assumption of 9° for the wedge angles of PtMn layer in our initial simulation was to clearly show the static spins and spin dynamics that help with the understanding of the underlying physics, and such assumption did not change the physics involved.

It should be noted that there was no shape anisotropy or demagnetizing field for the perfect and uniform antiferromagnet due to the zero net magnetization. However, as discussed earlier, size-induced missing coordination and the uncompensated moments, coupled with wedged shape, generated an effective asymmetric shape anisotropy [34–39], which tilted the moments in the PtMn layer as shown in Figs. 6(a) and 6(b). Meanwhile, a tilting angle of moments in the Co layer was caused by the interlayer exchange coupling. These effects created an effective in-plane field in the Co layer, resulting in field-free switching. On the other hand, applied *in situ* magnetic fields along $\pm y$ directions were able to enlarge or reduce the spin tilting angle of PtMn layer, leading to the enhancement or reduction of β_{DL} as observed.

IV. CONCLUSION

We demonstrated that the Pt/Co/PtMn heterostructures with wedged ultrathin AFM PtMn layer is an effective way to achieve field-free magnetization switching via breaking the lateral structural symmetry. We further found that the dampinglike fields (H_{DL}) are enhanced with the wedged ultrathin AFM PtMn layer by a percentage up to 30%. We conclude that the β_{DL} enhancement is possibly from noncollinear spin configuration at the interface caused by the wedged AFM PtMn layer. Micromagnetic simulations indicate the lateral structural symmetry breaking induced by the coupled effect of the missing coordination, the uncompensated moments, and the wedged shape in the PtMn layer play an important role in field-free switching. Our findings may advance the practical applications of SOT systems in ultralow-power and scalable spintronic memory and logic circuits.

It is worthy to note that in the current investigation, the wedge was formed due to varied substrate-to-target distance using lab-level tool. However, for practical applications, controlling thickness gradients across billions of devices across a whole wafer using such lab-level research tool is a rather demanding task. On the other hand, with advanced industrial sputtering tools, it is possible to deposit wedged film with varied thicknesses across a whole 8-inch wafer. Nevertheless, it is still a big challenge for the present technology to go for practical applications, and such challenge calls for intensive tool and technology development for precisely controlling the thickness gradient across a whole wafer and minimizing device-to-device variations.

ACKNOWLEDGMENTS

This work was supported by the "Pioneer" and "Leading Goose" R&D Program of Zhejiang Province under Grant No. 2022C01053, the National Natural Science Foundation of China (Grants No. 12004090 and No. 12104119), Key Research and Development Program of Zhejiang Province (Grant No. 2021C01039), Natural Science Foundation of Zhejiang Province, China (Grant No. LQ20F040005), and Zhejiang Provincial Natural Science Foundation (Grants No. LQ20F040005 and No. LQ21A050001).

[1] J. Liu, T. Xu, H. Feng, L. Zhao, J. Tang, L. Fang, and W. Jiang, Compensated ferrimagnet based artificial synapse and neuron for ultrafast neuromorphic computing, Adv. Funct. Mater. **32**, 2107870 (2022).

[2] R. Saha, K. Wu, R. P. Bloom, S. Liang, D. Tonini, and J. P. Wang, A review on magnetic and spintronic neurostimulation: Challenges and prospects, Nanotechnology **33**, 182004 (2022).

[3] R. Xie, S. Wang, L. Cai, X. Cui, S. Liu, Q. Cao, C. Zhang, Q. Huang, and S. Yan, Memristive switching by bulk spin–orbit torque in symmetry-broken ferromagnetic films, Appl. Phys. Lett. **120**, 192403 (2022).

[4] V. Lopez-Dominguez, Y. Shao, and P. Khalili Amiri, Perspectives on field-free spin–orbit torque devices for memory and computing applications, J. Appl. Phys. **133**, 040902 (2023).

[5] R. Maddu, D. Kumar, S. Bhatti, and S. N. Piramanayagam, Spintronic heterostructures for artificial intelligence: A materials perspective, Phys. Status Solidi RRL **17**, 2200493 (2023).

[6] X. H. Liu, K. W. Edmonds, Z. P. Zhou, and K. Y. Wang, Tuning Interfacial Spins in Antiferromagnetic–Ferromagnetic–Heavy-Metal Heterostructures Via Spin-Orbit Torque, Phys. Rev. Appl. **13**, 014059 (2020).

[7] P. He, X. Qiu, V. L. Zhang, Y. Wu, M. H. Kuok, and H. Yang, Continuous tuning of the magnitude and direction of spin-orbit torque using bilayer heavy metals, Adv. Electron. Mater. **2**, 1600210 (2016).

[8] L. Liu, T. Moriyama, D. C. Ralph, and R. A. Buhrman, Spin-torque Ferromagnetic Resonance Induced by the Spin Hall Effect, Phys. Rev. Lett. **106**, 036601 (2011).

[9] C. Zhang, S. Fukami, H. Sato, F. Matsukura, and H. Ohno, Spin-orbit torque induced magnetization switching in nanoscale Ta/CoFeB/MgO, Appl. Phys. Lett. **107**, 012401 (2015).

[10] C. Zhang, S. Fukami, K. Watanabe, A. Ohkawara, S. DuttaGupta, H. Sato, F. Matsukura, and H. Ohno, Critical role of W deposition condition on spin-orbit torque induced magnetization switching in nanoscale W/CoFeB/MgO, Appl. Phys. Lett. **109**, 192405 (2016).

[11] T. Chen, W. Liao, T. Chen, T. Tsai, C. Peng, and C. Pai, Current-induced spin–orbit torque efficiencies in W/Pt/Co/Pt heterostructures, Appl. Phys. Lett. **116**, 072405 (2020).

[12] C. Pai, L. Liu, Y. Li, H. W. Tseng, D. C. Ralph, and R. A. Buhrman, Spin transfer torque devices utilizing the giant spin Hall effect of tungsten, Appl. Phys. Lett. **101**, 122404 (2012).

[13] S. Fukami, C. Zhang, S. DuttaGupta, A. Kurenkov, and H. Ohno, Magnetization switching by spin-orbit torque in an antiferromagnet-ferromagnet bilayer system, Nat. Mater. **15**, 535 (2016).

[14] G. Yu, L.-T. Chang, M. Akyol, P. Upadhyaya, C. He, X. Li, K. L. Wong, P. K. Amiri, and K. L. Wang, Current-driven perpendicular magnetization switching in Ta/CoFeB/[TaO_x or MgO/TaO_x] films with lateral structural asymmetry, Appl. Phys. Lett. **105**, 102411 (2014).

[15] T. Jin, G. J. Lim, H. Y. Poh, S. Wu, F. Tan, and W. S. Lew, Spin reflection-induced field-free magnetization switching in perpendicularly magnetized MgO/Pt/Co heterostructures, ACS Appl. Mater. Interfaces **14**, 9781 (2022).

[16] A. van den Brink, G. Vermijs, A. Solignac, J. Koo, J. T. Kohlhepp, H. J. M. Swagten, and B. Koopmans, Field-free magnetization reversal by spin-Hall effect and exchange bias, Nat. Commun. **7**, 10854 (2016).

[17] K. Grochot, Ł. Karwacki, S. Łazarski, W. Skowroński, J. Kanak, W. Powroźnik, P. Kuświk, M. Kowacz, F. Stobiecki, and T. Stobiecki, Current-Induced Magnetization Switching of Exchange-Biased NiO Heterostructures Characterized by Spin-Orbit Torque, Phys. Rev. Appl. **15**, 014017 (2021).

[18] L. You, O. Lee, D. Bhowmik, D. Labanowski, J. Hong, J. Bokor, and S. Salahuddin, Switching of perpendicularly polarized nanomagnets with spin orbit torque without an external magnetic field by engineering a tilted anisotropy, Proc. Natl. Acad. Sci. USA **112**, 10310 (2015).

[19] Y. C. Lau, D. Betto, K. Rode, J. M. Coey, and P. Stamenov, Spin-orbit torque switching without an external field using interlayer exchange coupling, Nat. Nanotechnol. **11**, 758 (2016).

[20] W. Y. Kwak, J. H. Kwon, P. Grunberg, S. H. Han, and B. K. Cho, Current-induced magnetic switching with spin-orbit torque in an interlayer-coupled junction with a Ta spacer layer, Sci. Rep. **8**, 3826 (2018).

[21] Y. Sheng, K. W. Edmonds, X. Ma, H. Zheng, and K. Wang, Adjustable current-induced magnetization switching utilizing interlayer exchange coupling, Adv. Electron. Mater. **4**, 1800224 (2018).

[22] W. J. Kong, C. H. Wan, X. Wang, B. S. Tao, L. Huang, C. Fang, C. Y. Guo, Y. Guang, M. Irfan, and X. F. Han, Spin-orbit torque switching in a T-type magnetic configuration with current orthogonal to easy axes, Nat. Commun. **10**, 233 (2019).

[23] H. Wu, J. Nance, S. A. Razavi, D. Lujan, B. Dai, Y. Liu, H. He, B. Cui, D. Wu, K. Wong, K. Sobotkiewich, X. Li, G. P. Carman, and K. L. Wang, Chiral symmetry breaking for deterministic switching of perpendicular magnetization by spin-orbit torque, Nano Lett. **21**, 515 (2021).

[24] G. Yu, P. Upadhyaya, Y. Fan, J. G. Alzate, W. Jiang, K. L. Wong, S. Takei, S. A. Bender, L. T. Chang, Y. Jiang, M. Lang, J. Tang, Y. Wang, Y. Tserkovnyak, P. K. Amiri, and K. L. Wang, Switching of perpendicular magnetization by spin-orbit torques in the absence of external magnetic fields, Nat. Nanotechnol. **9**, 548 (2014).

[25] B. Cui, H. Wu, D. Li, S. A. Razavi, D. Wu, K. L. Wong, M. Chang, M. Gao, Y. Zuo, L. Xi, and K. L. Wang, Field-free spin–orbit torque switching of perpendicular magnetization by the Rashba interface, ACS Appl. Mater. Interfaces **11**, 39369 (2019).

[26] D. Li, B. Cui, X. Guo, Z. Xiao, W. Zhang, X. Jia, J. Duan, X. Liu, J. Chen, Z. Quan, G. Yu, and X. Xu, Field-free spin–orbit torque driven multi-state reversal in wedged Ta/MgO/CoFeB/MgO heterostructures, APL Mater. **9**, 071108 (2021).

[27] C.-F. Pai, M. Mann, A. J. Tan, and G. S. D. Beach, Determination of spin torque efficiencies in heterostructures with perpendicular magnetic anisotropy, Phys. Rev. B **93**, 144409 (2016).

[28] B. Cui, Z. Zhu, C. Wu, X. Guo, Z. Nie, H. Wu, T. Guo, P. Chen, D. Zheng, T. Yu, L. Xi, Z. Zeng, S. Liang, G. Zhang, G. Yu, and K. L. Wang, Comprehensive study of the current-induced spin-orbit torque perpendicular effective field in asymmetric multilayers, Nanomaterials **12**, 1887 (2022).

[29] T.-Y. Chen, H.-I. Chan, W.-B. Liao, and C.-F. Pai, Current-Induced Spin-Orbit Torque and Field-Free Switching in Mo-Based Magnetic Heterostructures, Phys. Rev. Appl. **10**, 044038 (2018).

[30] A. Razavi, H. Wu, B. Dai, H. He, D. Wu, K. Wong, G. Yu, and K. L. Wang, Spin-orbit torques in structures with asymmetric dusting layers, Appl. Phys. Lett. **117**, 182403 (2020).

[31] A. Razavi, H. Wu, Q. Shao, C. Fang, B. Dai, K. Wong, X. Han, G. Yu, and K. L. Wang, Deterministic spin-orbit torque switching by a light-metal insertion, Nano Lett. **20**, 3703 (2020).

[32] S. Chen, R. Mishra, H. Chen, H. Yang, and X. Qiu, Mimicking synaptic plasticity with a wedged Pt/Co/Pt spin–orbit torque device, J. Phys. D: Appl. Phys. **55**, 095001 (2021).

[33] R. Chen, Q. Cui, L. Liao, Y. Zhu, R. Zhang, H. Bai, Y. Zhou, G. Xing, F. Pan, H. Yang, and C. Song, Reducing Dzyaloshinskii-Moriya interaction and field-free spin-orbit torque switching in synthetic antiferromagnets, Nat. Commun. **12**, 3113 (2021).

[34] M. Bode, E. Y. Vedmedenko, K. von Bergmann, A. Kubetzka, P. Ferriani, S. Heinze, and R. Wiesendanger, Atomic spin structure of antiferromagnetic domain walls, Nat. Mater. **5**, 477 (2006).

[35] M. Gruyters and D. Schmitz, Microscopic Nature of Ferro- and Antiferromagnetic Interface Coupling of Uncompensated Magnetic Moments in Exchange Bias Systems, Phys. Rev. Lett. **100**, 077205 (2008).

[36] T. Kosub, M. Kopte, F. Radu, O. G. Schmidt, and D. Makarov, All-Electric Access to the Magnetic-Field-Invariant Magnetization of Antiferromagnets, Phys. Rev. Lett. **115**, 097201 (2015).

[37] P. N. Lapa, I. V. Roshchin, J. Ding, J. E. Pearson, V. Novosad, J. S. Jiang, and A. Hoffmann, Magnetoresistive detection of strongly pinned uncompensated magnetization in antiferromagnetic FeMn, Phys. Rev. B **95**, 020409(R) (2017).

[38] A. Mougin, J. Borme, R. L. Stamps, A. Marty, P. Bayle-Guillemaud, Y. Samson, and J. Ferré, Antiferromagnetic relaxation and induced anisotropy in Fe/twinned-PtMn bilayers, Phys. Rev. B **73**, 024401 (2006).

[39] M. Charilaou and F. Hellman, Roughness effects in uncompensated antiferromagnets, J. Appl. Phys. **117**, 083907 (2015).

[40] H. Wu, J. Zhang, B. Cui, S. A. Razavi, X. Che, Q. Pan, D. Wu, G. Yu, X. Han, and K. L. Wang, Field-free approaches for deterministic spin–orbit torque switching of the perpendicular magnet, Mater. Futures **1**, 022201 (2022).

[41] X. Shu, L. Liu, J. Zhou, W. Lin, Q. Xie, T. Zhao, C. Zhou, S. Chen, H. Wang, J. Chai, Y. Ding, W. Chen, and J. Chen, Field-Free Switching of Perpendicular Magnetization Induced by Longitudinal Spin-Orbit-Torque Gradient, Phys. Rev. Appl. **17**, 024031 (2022).

[42] B. Wu, M. Jin, Y. Luo, X. Xu, H. Fan, H. Huang, Z. Feng, Y. Zhuang, C. Yu, and T. Zhou, Enhancement of damping-like field and field-free switching in Pt/(Co/Pt)/PtMn trilayer films prepared in the presence of an *in situ* magnetic field, ACS Appl. Mater. Interfaces **14**, 21668 (2022).

[43] L. Liu, C. Zhou, X. Shu, C. Li, T. Zhao, W. Lin, J. Deng, Q. Xie, S. Chen, J. Zhou, R. Guo, H. Wang, J. Yu, S. Shi, P. Yang, S. Pennycook, A. Manchon, and J. Chen, Symmetry-dependent field-free switching of perpendicular magnetization, Nat. Nanotechnol. **16**, 277 (2021).

[44] H. Wu, P. Zhang, P. Deng, Q. Lan, Q. Pan, S. A. Razavi, X. Che, L. Huang, B. Dai, K. Wong, X. Han, and K. L. Wang, Room-Temperature Spin-Orbit Torque from Topological Surface States, Phys. Rev. Lett. **123**, 207205 (2019).

[45] See Supplemental Material at http://link.aps.org/supplemental/10.1103/PhysRevB.108.054417 for the ANE contribution; the current-shunting effect; the XRD and crystal structure of the sample; the simulated R-I loops for wedged PtMn sample; the anisotropy energy; and the demagnetization energy. It also contains Refs. [46–49].

[46] G. Kresse and J. Hafner, *Ab initio* molecular dynamics for liquid metals, Phys. Rev. B **47**, 558 (1993).

[47] G. Kresse and J. Furthmüller, Efficient iterative schemes for *ab initio* total-energy calculations using a plane-wave basis set, Phys. Rev. B **54**, 11169 (1996).

[48] Y. Wang, J. Lv, L. Zhu, and Y. Ma, Crystal structure prediction via particle-swarm optimization, Phys. Rev. B **82**, 094116 (2010).

[49] Y. Wang, J. Lv, L. Zhu, and Y. Ma, CALYPSO: A method for crystal structure prediction, Comput. Phys. Commun. **183**, 2063 (2012).

[50] H. V. Gomonay and V. M. Loktev, Spin transfer and current-induced switching in antiferromagnets, Phys. Rev. B **81**, 144427 (2010).

[51] X. Xu, Y. G. Semenov, and K. W. Kim, Electrical generation and propagation of spin waves in antiferromagnetic thin-film nanostrips, Appl. Phys. Lett. **114**, 232403 (2019).

[52] X.-L. Li, X. Duan, Y. G. Semenov, and K. W. Kim, Electrical switching of antiferromagnets via strongly spin-orbit coupled materials, J. Appl. Phys. **121**, 023907 (2017).

[53] Y.-C. Liao, D. E. Nikonov, S. Dutta, S.-C. Chang, S. Manipatruni, I. A. Young, and A. Naeemi, Simulation of the magnetization dynamics of a single-domain $BiFeO_3$ nanoisland, IEEE Trans. Magn. **56**, 1 (2020).

[54] N. S. Gusev, A. V. Sadovnikov, S. A. Nikitov, M. V. Sapozhnikov, and O. G. Udalov, Manipulation of the Dzyaloshinskii-Moriya Interaction in Co/Pt Multilayers with Strain, Phys. Rev. Lett. **124**, 157202 (2020).

[55] C. Eyrich, W. Huttema, M. Arora, E. Montoya, F. Rashidi, C. Burrowes, B. Kardasz, E. Girt, B. Heinrich, O. N. Mryasov, M. From, and O. Karis, Exchange stiffness in thin film Co alloys, J. Appl. Phys. **111**, 07C919 (2012).

[56] S. Mizukami, E. P. Sajitha, D. Watanabe, F. Wu, T. Miyazaki, H. Naganuma, M. Oogane, and Y. Ando, Gilbert damping in perpendicularly magnetized Pt/Co/Pt films investigated by all-optical pump-probe technique, Appl. Phys. Lett. **96**, 152502 (2010).